Supplemental material for

Ultrafast broadband optical spectroscopy for quantifying subpicometric coherent atomic displacements in WTe$_2$

Davide Soranzio,[1] Maria Peressi,[1] Robert J. Cava,[2]

Fulvio Parmigiani,[1, 3, 4] and Federico Cilento[4, *]

[1]*Dipartimento di Fisica, Università degli Studi di Trieste, 34127 Trieste, Italy*

[2]*Department of Chemistry, Princeton University,*

Princeton, New Jersey 08544, USA

[3]*International Faculty, University of Cologne,*

Albertus-Magnus-Platz, 50923 Cologne, Germany

[4]*Elettra-Sincrotrone Trieste S.C.p.A., 34149 Basovizza, Italy*

(Dated: November 4, 2019)

PART 1 - CRYSTAL STRUCTURE OF TUNGSTEN DITELLURIDE

In Fig. S1, ball-and-stick projections of the crystal structure of the layered orthorhombic phase of tungsten ditelluride (WTe_2) are shown. The crystallographic data were taken from [1]. All the crystallographic representations were generated using the XCrySDen [2] software.
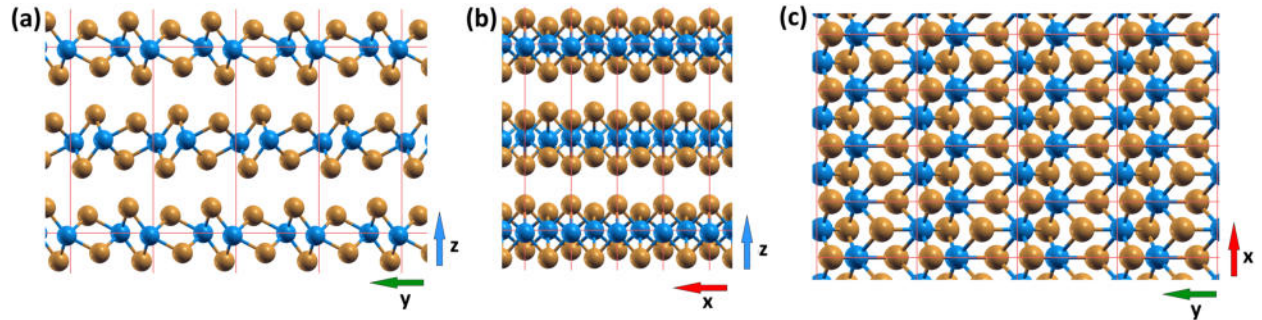

FIG. S1. Projections of WTe_2 crystal structure perpendicular to the (a) $\mathbf{x}$, (b) $\mathbf{y}$ and (c) $\mathbf{z}$ (only a single layer is shown) axes; $\mathbf{x}$ and $\mathbf{y}$ are the perpendicular in-plane directions, while the $\mathbf{z}$ axis is perpendicular to the layers; tungsten atoms in blue, tellurium atoms in orange; the unit cells are delimited by red lines.

PART 2 - EXPERIMENTAL RESULTS

All the experiments were executed at the T-ReX laboratory at Elettra Sincrotrone Trieste. The time-resolved reflectivity experiments were performed using a Ti:sapphire femtosecond (fs) laser system, delivering, at a repetition rate of 250 kHz, ~50 fs light pulses at a wavelength of 800 nm (1.55 eV).

The output beam of the laser system was split into pump and probe beams which reunite at the sample. During their paths, the pump beam was delayed through a linear stage to control the pump-probe delay, while the probe beam was focused in a sapphire window to produce a broad (0.8-2.3 eV) supercontinuum spectrum. On the sample, the pump spot diameter was estimated to be ~160 μm, while the average spot diameter for the various spectral components of the probe beam was ~110 μm. After reflection from the sample in quasi-normal conditions, the probe beam's spectral components are dispersed through a glass prism and measured with an InGaAs photodiode array (PDA).
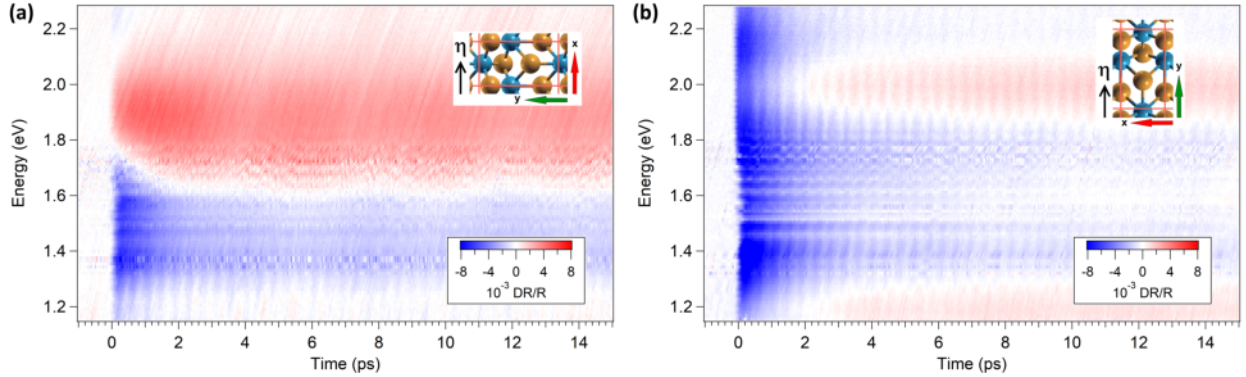
FIG. S2. (a),(b) Data obtained with a 1.03 eV pump photon energy, taken at $\sim$490 μJ/cm^2 absorbed pump fluence and T=295 K respectively for $\eta||\mathbf{x}$ and $\eta||\mathbf{y}$.

Modifying the pump polarization direction produced no significant variation of the main spectral features. For this reason, all measurements were performed by keeping the pump beam polarization perpendicular to the probe one, in order to minimize the residual pump scattering by using a polarizer inserted before the detectors.

Error intervals are expressed as $\pm\sigma$, one standard deviation.

2.1 - Measurement at 1.03 eV pump photon energy

In order to check that the reflectivity variation DR/R is independent from the pump photon energy, we repeated part of the measurements by pumping at 1.03 eV photon energy (Fig. S2), obtained thanks to an optical parametric amplifier (OPA). We verified that the DR/R is qualitatively similar to the results obtained with the 1.55 eV (800 nm) excitation. Moreover, since in this experimental condition the pump lies at the edge of the measured spectral range, the spectral region around 1.55 eV is not covered by scattered pump photons. This allowed us to confirm that no structured features are present in this range, that was hidden in the datasets of the main paper acquired with 1.55 eV pump photon energy (Figs. 1(c),(d), main paper).

2.2 - Time-domain analysis

In Fig. S3 we report selected profiles extracted at two photon energies from the datasets reported in Figs. 1(c),(d) in the main paper, alongside with the Fast Fourier Transform
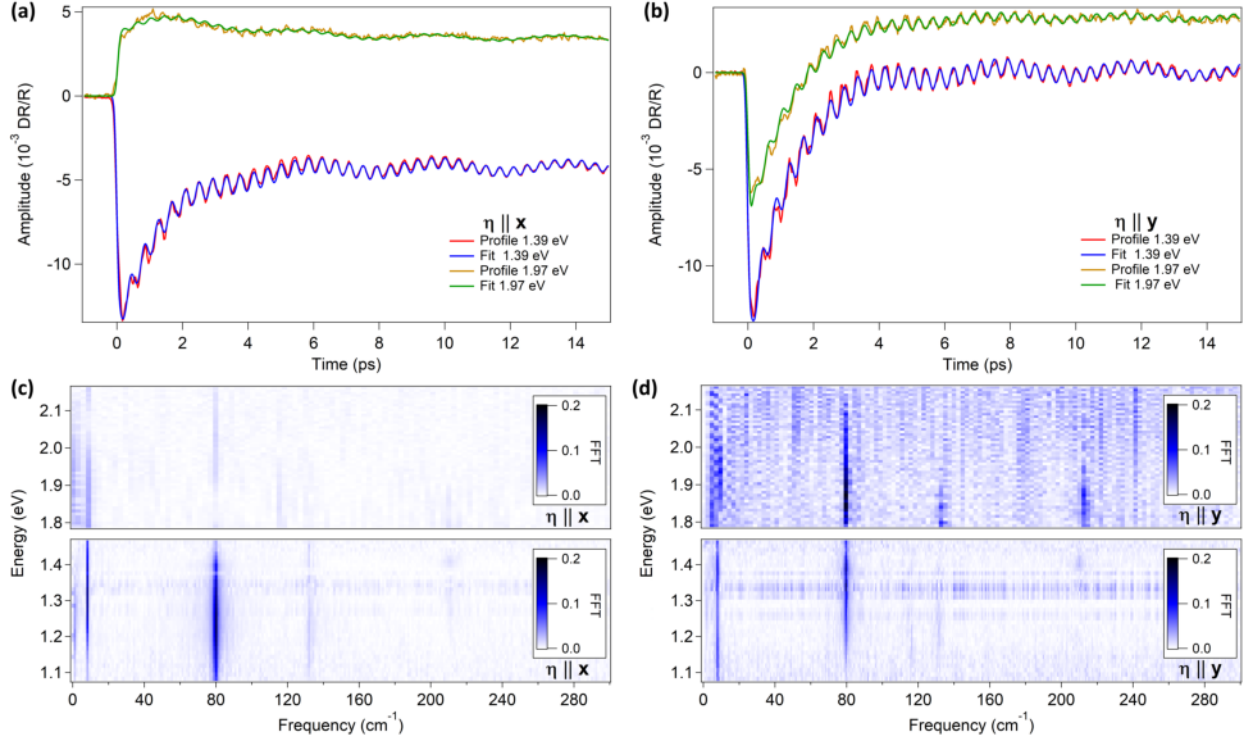
3

FIG. S3. Profiles at 1.39 eV and 1.97 eV photon energy for probe beam polarization (a) $\eta||\mathbf{x}$ and (b) $\eta||\mathbf{y}$, at $\sim$710 μJ/cm^2 absorbed pump fluence and T=295 K. Fast Fourier Transform images performed across a few picoseconds after time zero for (c) $\eta||\mathbf{x}$ and (d) $\eta||\mathbf{y}$ after subtracting from the data a purely exponential fit based on Eq. (1) in the main paper for various probe photon energies.
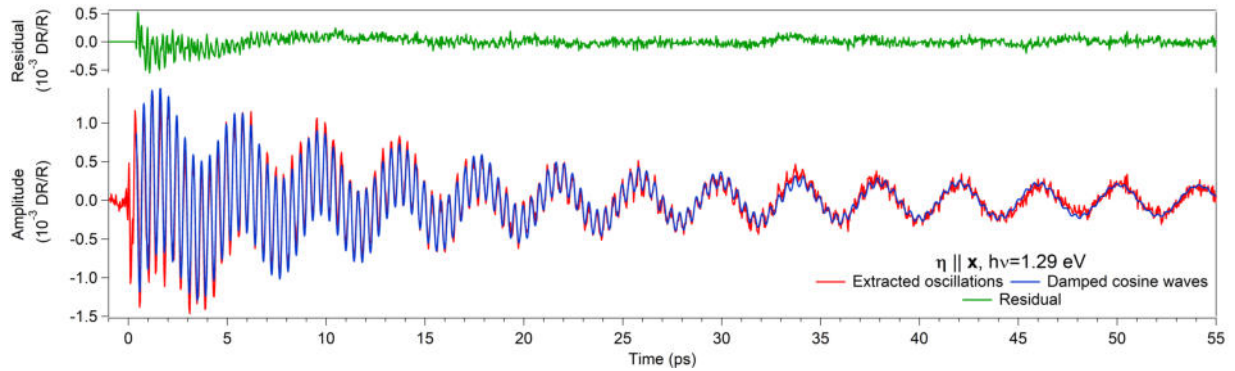

FIG. S4. Oscillatory component of the DR/R signal, obtained by subtracting an exponential fit (see Eq. (1) in the main paper) from the temporal profile at 1.29 eV acquired at $\sim$710 μJ/cm^2 absorbed pump fluence and T=295 K for $\eta||\mathbf{x}$.

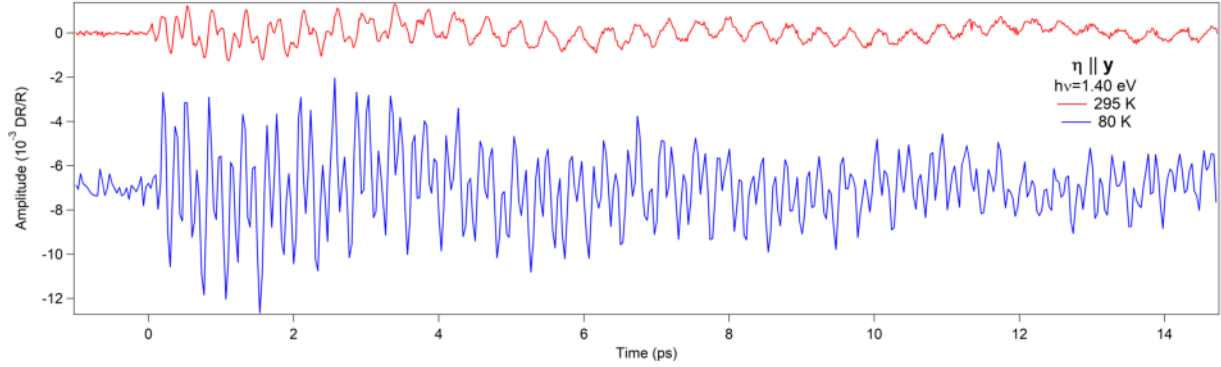(FFT) of the oscillatory signal in most of the investigated range. The most prominent

FIG. S5. Phonon modulation of DR/R, obtained by subtracting an exponential fit (see Eq. (1) in the main paper) from the temporal profiles at 1.40 eV acquired at $\sim$710 µJ/cm^2 absorbed pump fluence, T=80 K and T=295 K and for $\eta||\mathbf{y}$; the beats are due to phonon modes with frequency higher than 80 cm^{-1}.

features are at $\sim$8 and 80 cm^{-1}. These modes give the largest contribution to the coherent component of the DR/R signal as shown in Fig. S4, where two damped cosine waves fit the oscillatory signal. Minor contributions at higher frequencies ($\sim$117, 132 and 210 cm^{-1}) are detected and appear as beats in the oscillatory signal. Their contribution becomes more relevant as the temperature is reduced (Fig. S5).

In the visible spectral region (1.70-2.10 eV), the DR/R cannot be fitted by a single exponential decay (Eq. (1) in the main paper) for probe polarization $\eta||\mathbf{x}$. In presence of contributions with opposite sign and comparable time constants, the DR/R reaches its maximum value at longer delay, analogously to the case in Fig. S3(a). This delay can be as large as 1 ps, alongside with a slower decay of the signal. Investigating the dependence on fluence, we learned that (Fig. S6) the delay increases with the deposited pump energy. At variance, in the infrared the peak position is independent on the fluence. For this reason, for example, it is not possible to effectively describe the behavior of this material with just a single Drude-Lorentz term [3] in the dielectric tensor for the measured spectral range. For $\eta||\mathbf{y}$, we do not observe such phenomenon. This may be connected to different matrix elements for the involved transitions in the two distinct linear probe polarizations.
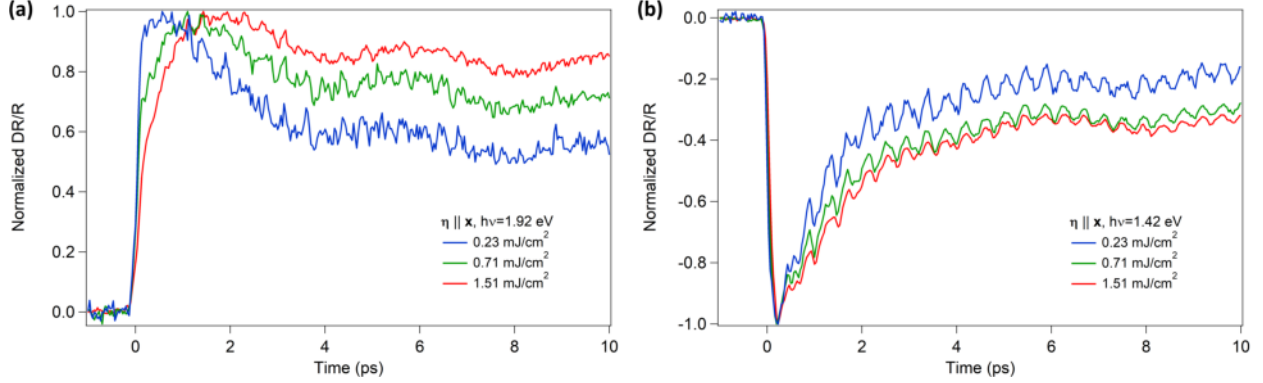
5

FIG. S6. DR/R profiles obtained from 1.55 eV pump photon energy-broadband supercontinuum probe beam experiments at different fluences and T=295 K for probe polarization $\eta||\mathbf{x}$; the profiles in (a) at 1.92 eV show a fluence-dependent position of the main out-of-equilibrium peak, while the profiles in (b) at 1.42 eV do not present such behavior.

2.3 - Low fluence and low temperature measurements

The DR/R broadband image measured at $\sim$230 μJ/cm^2 absorbed pump fluence and T=295 K (Fig. S7) presents the same characteristics of that measured at higher fluence (see Figs. 1(c), 3(a) and 4(a) in the main paper). Such features are also well captured by ab-initio results obtained with properly rescaled eigendisplacements.

At T=80 K, phonons exhibit a blueshift in their frequencies with respect to T=295 K, as previously reported in [4][5]. Compared to T=295 K the contribution from coherent phonons with frequency at higher than 80 cm^{-1} becomes more prominent in the DR/R images measured at $\sim$710 μJ/cm^2 (Figs. S8, S9) and $\sim$230 μJ/cm^2 (Fig. S10) absorbed pump fluence. The phonon effects for $\eta||\mathbf{x}$ shown in Fig. S11 are analogous to the room temperature results reported in Figs. 4(a), S7(d), although it becomes harder to separate them using the same method. This becomes especially challenging for $\eta||\mathbf{y}$, where the amplitude of phonons with frequency higher than 80 cm^{-1} is comparable to the lower modes (Fig. S5) throughout the investigated spectral region. In this case, a more advanced procedure involving a time-weighted average over multiple 0 or π phase profiles to determine the initial amplitudes of the atomic shifts could be employed.
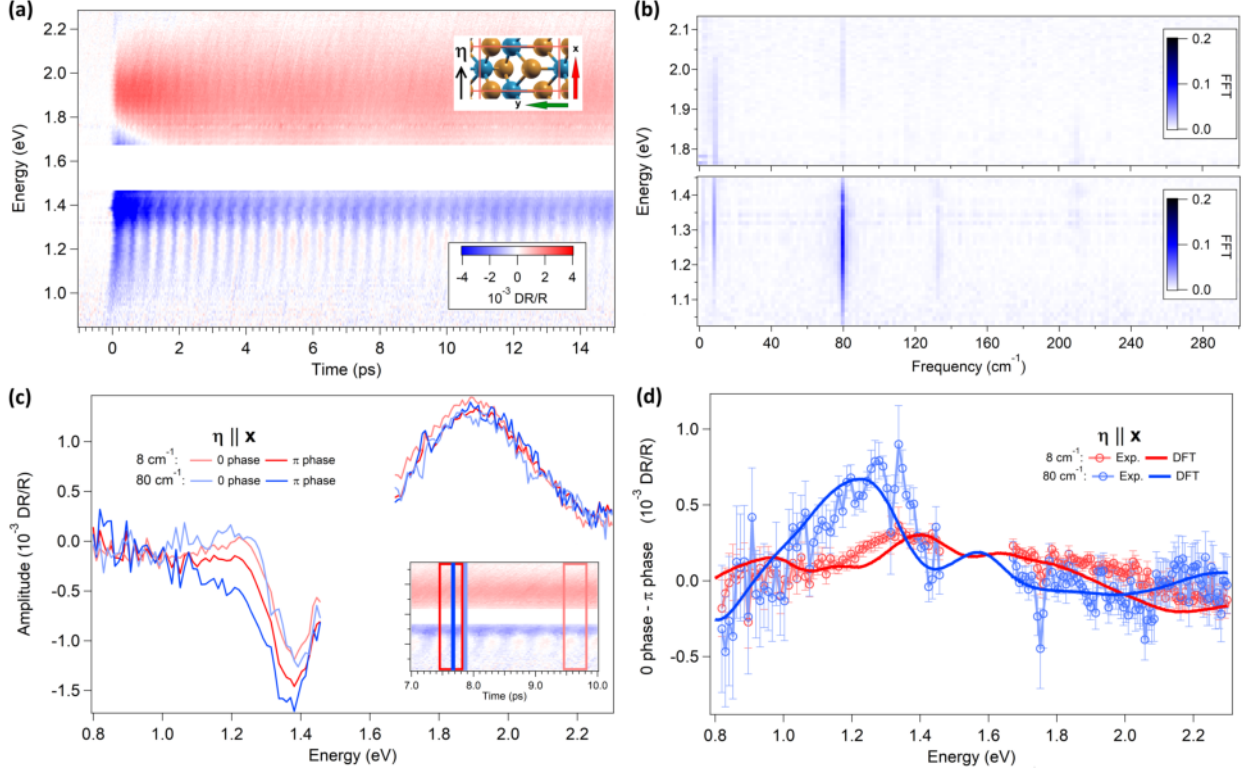
FIG. S7. (a) Ultrafast broadband DR/R image for WTe_2 for probe polarization $\eta||\mathbf{x}$ taken at $\sim$230 μJ/cm^2 absorbed pump fluence and T=295 K. (b) Fast Fourier Transform images performed across a few picoseconds after time zero after subtracting from the data a purely exponential fit based on Eq. (1) in the main paper. (c) Spectral profiles taken at selected time delays for maxima and minima of the 8 cm^{-1} and 80 cm^{-1} optical phonon effects; the inset, with the same vertical axis and color scale as (a), shows the exact temporal positions. (d) Comparisons between the experimental and DFT calculated DR/R difference between the 0 and π phases displayed in (c), showcasing the effects of the 8 cm^{-1} and 80 cm^{-1} optical phonons for $\eta||\mathbf{x}$.

2.4 - Ultrafast single-color probe optical spectroscopy

To investigate the response of the material as a function of the fluence, we performed a series of pump-probe reflectivity experiments at 1.03 eV pump and 1.55 eV probe photon energies. The results are summarized in Fig. S12. From Figs. S12(c),(f), it can be inferred that the amplitude of the main peak and of the phonon effects can be considered a linear function of the absorbed pump fluence in the whole investigated range within a very good approximation. Compared to the time-resolved broadband optical experiments, the 80 cm^{-1}
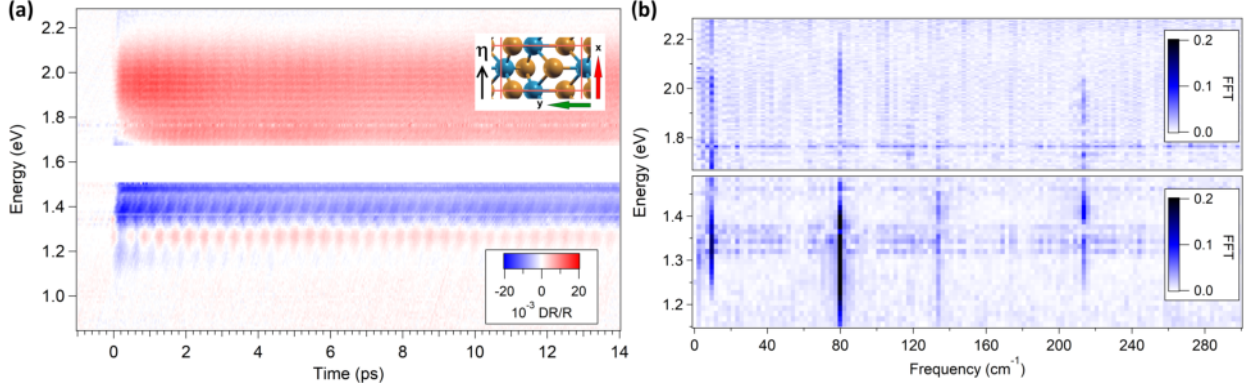
FIG. S8. (a) Ultrafast broadband DR/R image for WTe$_2$ for probe polarization $\eta||\mathbf{x}$ taken at $\sim$710 µJ/cm^2 absorbed pump fluence and T=80 K. (b) Fast Fourier Transform images performed across a few picoseconds after time zero after subtracting from the data a purely exponential fit based on Eq. (1) in the main paper for various probe photon energies.

FIG. S9. (a) Ultrafast broadband DR/R image for WTe$_2$ for probe polarization $\eta||\mathbf{y}$ taken at $\sim$710 µJ/cm^2 absorbed pump fluence and T=80 K. (b) Fast Fourier Transform images performed across a few picoseconds after time zero after subtracting from the data a purely exponential fit based on Eq. (1) in the main paper for various probe photon energies.
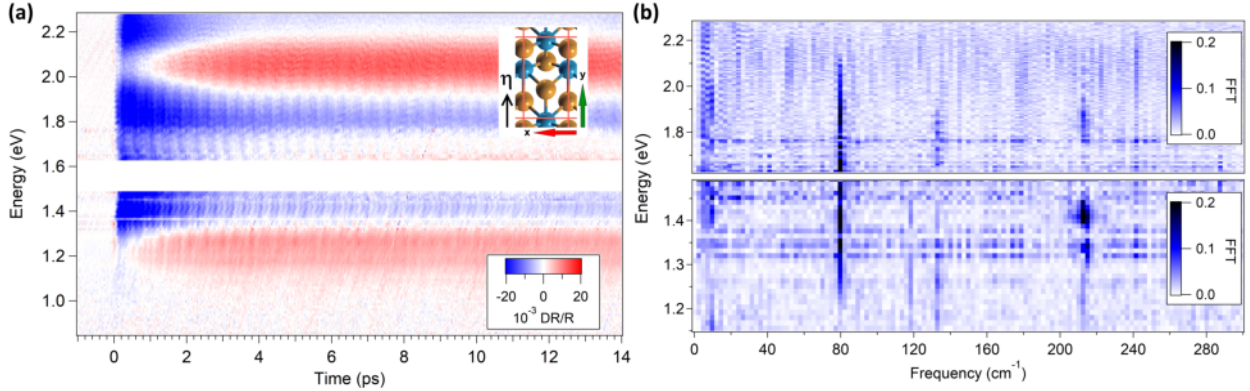
oscillations are quenched because of the following effect. The probe pulse (1.55 eV, 800 nm) produced by the amplifier has a wide bandwidth ($>$40 nm) with a finite residual chirp. This chirp cannot be resolved when the full bandwidth of the pulse is measured with a single photodiode, as it happens with lock-in acquisition, leading to a smearing of the fast oscillatory signal. We also want to stress the fact that only the DR/R as measured by broadband spectroscopy can be considered as quantitative. The DR/R magnitude measured through lock-in acquisition is smaller by a given factor, arising from the signal treatment
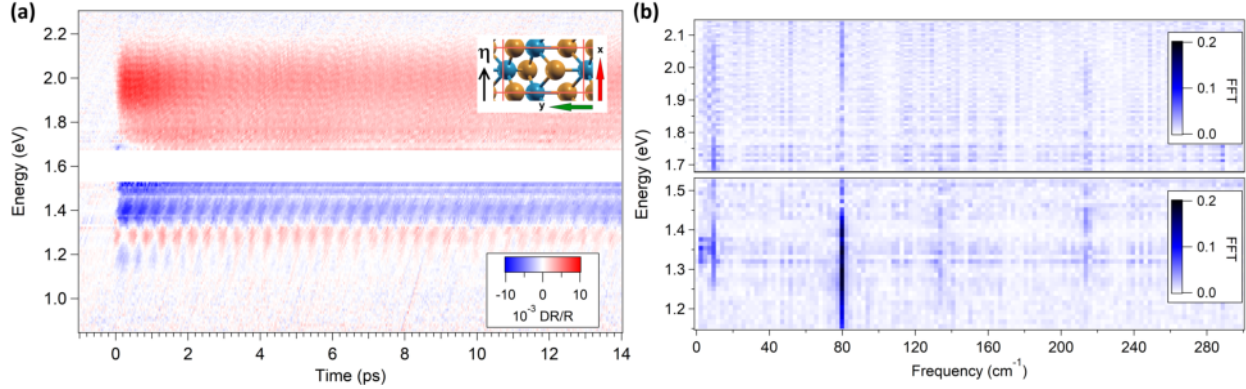
8

FIG. S10. (a) Ultrafast broadband DR/R image for WTe$_2$ for probe polarization $\eta||\mathbf{x}$ taken at $\sim$230 μJ/cm^2 absorbed pump fluence and T=80 K. (b) Fast Fourier Transform images performed across a few picoseconds after time zero after subtracting from the data a purely exponential fit based on Eq. (1) in the main paper for various probe photon energies.

introduced by the lock-in device.

Furthermore, it is possible to determine the timescale of the long-lasting offset observed in the time-resolved profiles. As shown in Fig. S13, the signal survives for hundreds of picoseconds. Its timescale reminds of similar long-lasting non-equilibrium signal observed in time-resolved x-ray diffraction and time-resolved electron diffraction for transition metals, ascribed to the transient lattice heating [6].
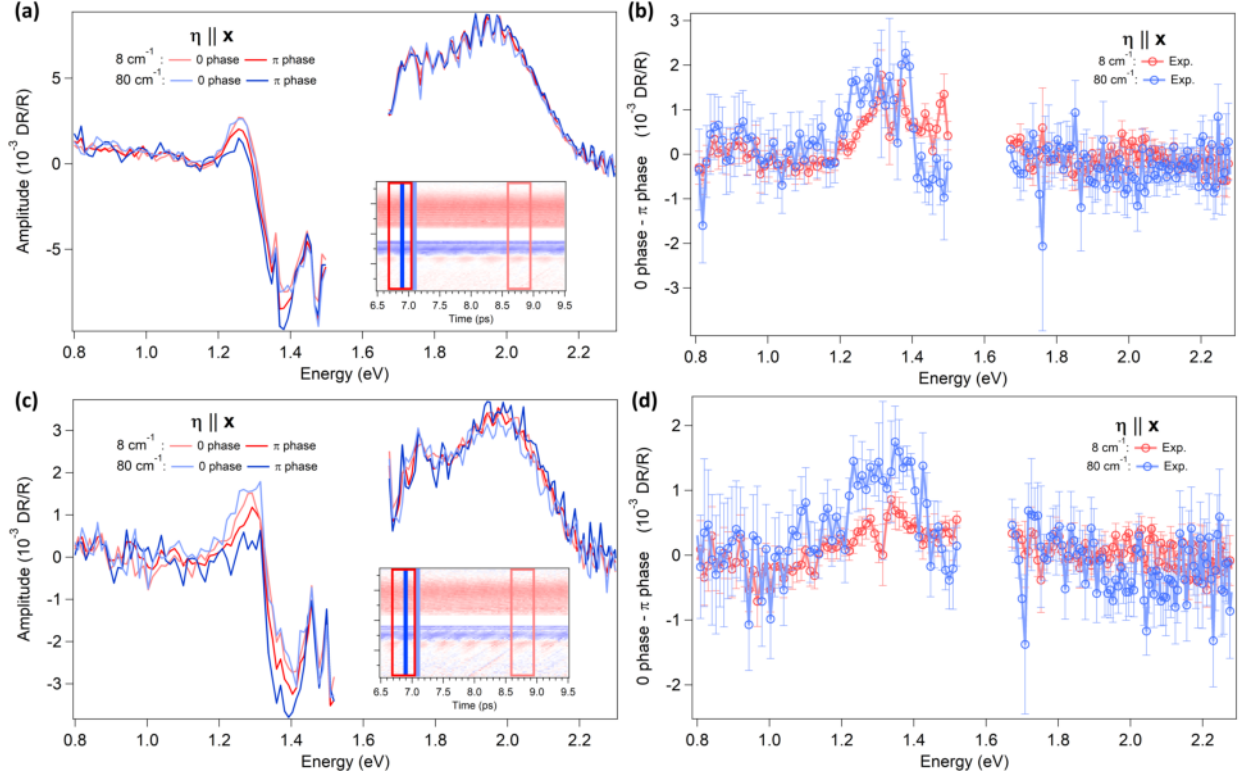
FIG. S11. Spectral profiles taken at selected time delays for maxima and minima of the 8 cm^{-1} and 80 cm^{-1} optical phonon effects taken at a) ~710, c) ~230 μJ/cm^2 absorbed pump fluence and T=80 K; the inset, with the same vertical axis and color scale as the corresponding graphs in Figs. S8, S10, shows the exact temporal positions. (b),(d) Experimental DR/R difference between the 0 and π phases displayed in respectively (a) and (c), showcasing the effects of the 8 cm^{-1} and 80 cm^{-1} optical phonons for $\eta||\mathbf{x}$.
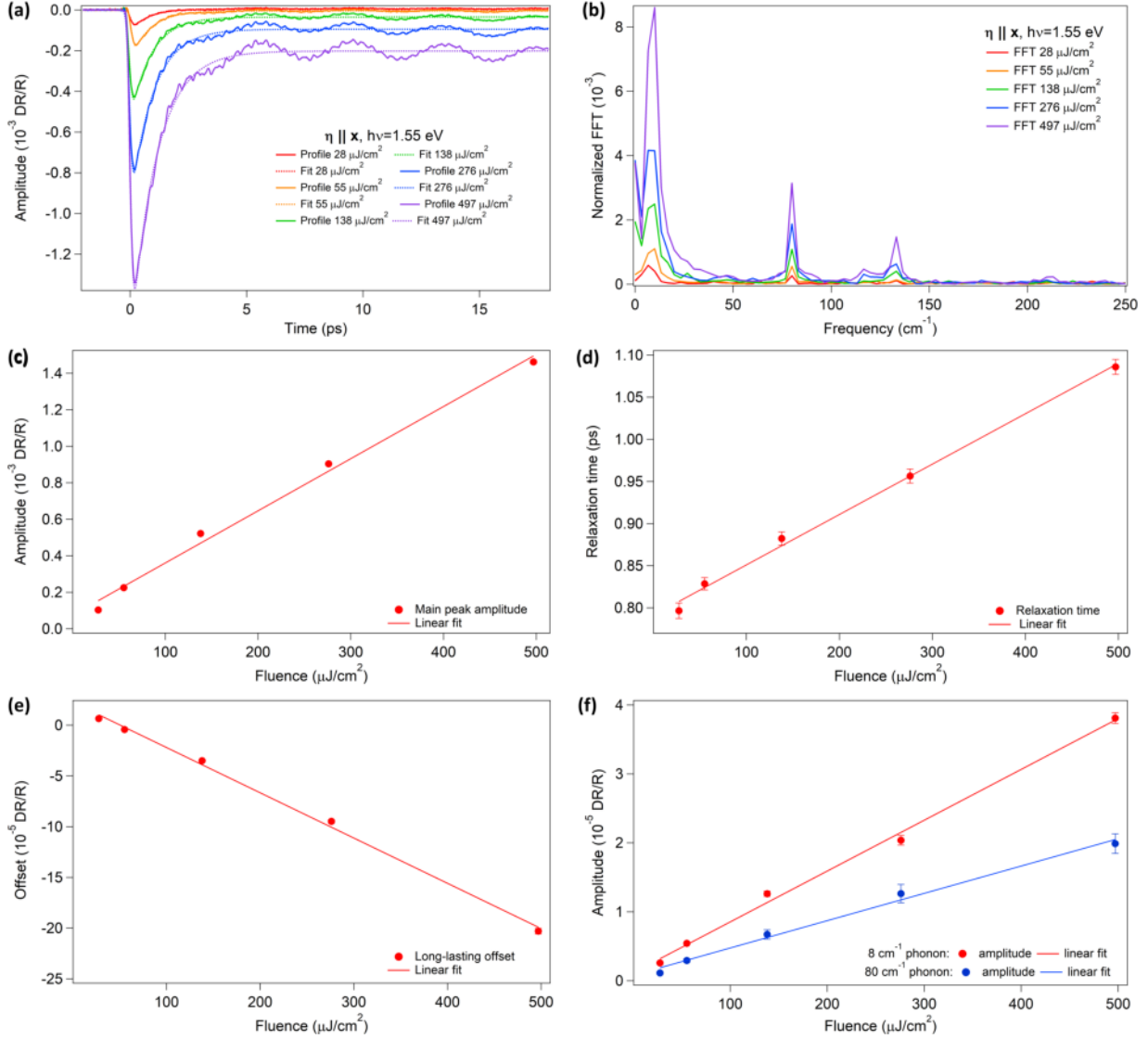
FIG. S12. (a) Absorbed fluence dependence on the out-of-equilibrium profiles performed with 1.03 eV pump and 1.55 eV single-color probe with $\eta||\mathbf{x}$, at T=295 K, where a single-exponential decay model was used to fit the curves; see Eq. (1) of the main paper for details. (b) Fast Fourier Transform (FFT) transform of the residual signals after subtracting to the profiles the fit function. Fit parameters of the single-exponential decay model obtained from the curves reported in panel (a) respectively for (c) amplitude and (d) relaxation time of the main peak, (e) offset and (f) amplitudes of the phonon effects related to the 8 cm^{-1} and 80 cm^{-1} modes. These last values represent the amplitude of two damped cosine waves fitted to the residual signals.
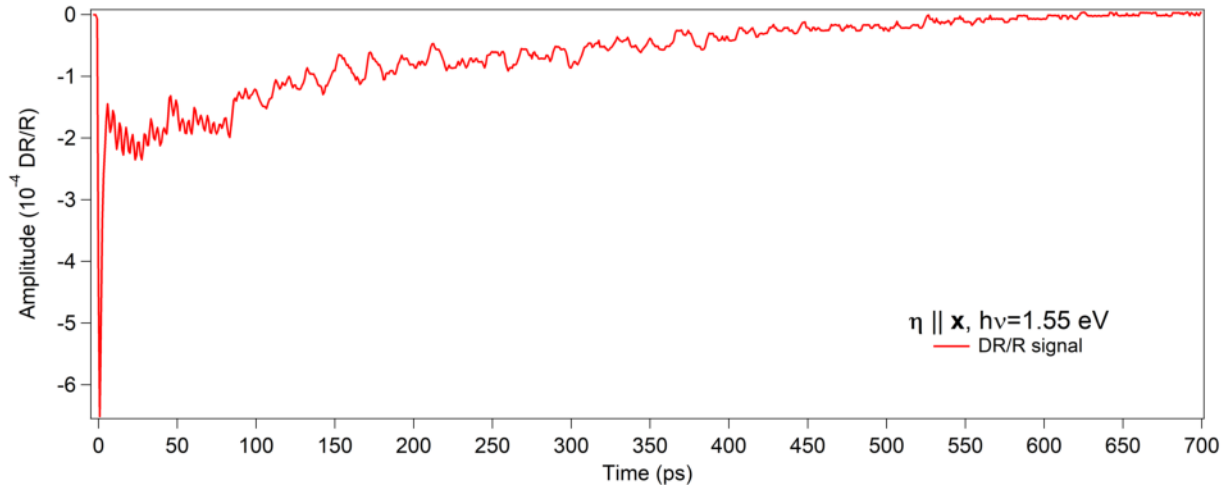
FIG. S13. Single-color DR/R curve obtained at 1.03 eV pump photon energy and a perpendicularly polarized 1.55 eV probe beam polarized along $\eta||\mathbf{x}$ at $\sim$500 μJ/cm^2 absorbed pump fluence and T=295 K, showing that the material returns to its equilibrium in about 700 ps.

PART 3 - COMPUTATIONAL RESULTS

Density functional theory (DFT) simulations were carried out using norm-conserving (NC) [7] scalar relativistic [8] pseudopotentials with the generalized gradient approximation (GGA) in the Perdew-Burke-Ernzerhof (PBE) parametrization for the exchange-correlation functional [9] chosen from the PseudoDojo database [10][11]. An orthorhombic simulation cell (Figs. S1(a)-(c)), with lattice constants a=3.477 Å, b=6.249 Å and c=14.018 Å along the $\mathbf{x}$, $\mathbf{y}$ and $\mathbf{z}$ directions respectively taken from the crystallographic data in [1], was used. It contains four tungsten and eight tellurium atoms, with 14 and 16 valence electrons respectively, for a total number of 184 electrons per unit cell.

Structural optimizations and phonon calculations in the framework of density functional perturbation theory (DFPT) were performed using the QUANTUM ESPRESSO (QE) [12] suite of codes with a plane wave kinetic energy cutoff of 70 Rydberg and a 12×10×6 uniform k-point mesh for integrations over the Brillouin zone. Van der Waals contributions were not included, since, although in general relevant to describe layered compounds, in this specific case they do not improve the description of structural and electronic/optical properties of the system.

Td-WTe$_2$ presents 33 zone-center optical phonon modes with four possible symmetry representations given by the C$_{2v}$ point group [1]. In the following sections, we will focus on the two lowest energy A$_1$ modes. We calculated the diagonal macroscopic dielectric tensor components through the YAMBO code [13] starting from the wavefunctions and eigenvalues obtained through the PW package of QE using the same kinetic energy cut-off and a 16×14×10 k-grid. Convergence tests showed that these parameters ensure the numerical accuracy needed to appreciate the relative effects of subpicometer atomic displacements on the electronic states in the near-infrared and visible spectral regions. The number of conduction bands to be considered in the calculations was also determined from convergence tests. The reflectance curves were derived at the independent-particle (IP) level using a linear response approach.

3.1 - Equilibrium reflectance

We report the calculated reflectance curves along the two perpendicular polarization directions in Fig. S14, compared with the reflectance data found in [14]. We included 119 bands for the response function to reproduce the experimental data with a very good quantitative agreement. Although the experimental data was measured at 10 K and DFT results were obtained at T=0 K, they can be still considered adequate for our DR/R comparisons at T=295 K in good approximation, since the optical properties in this spectral region are only slightly affected by temperature [15].
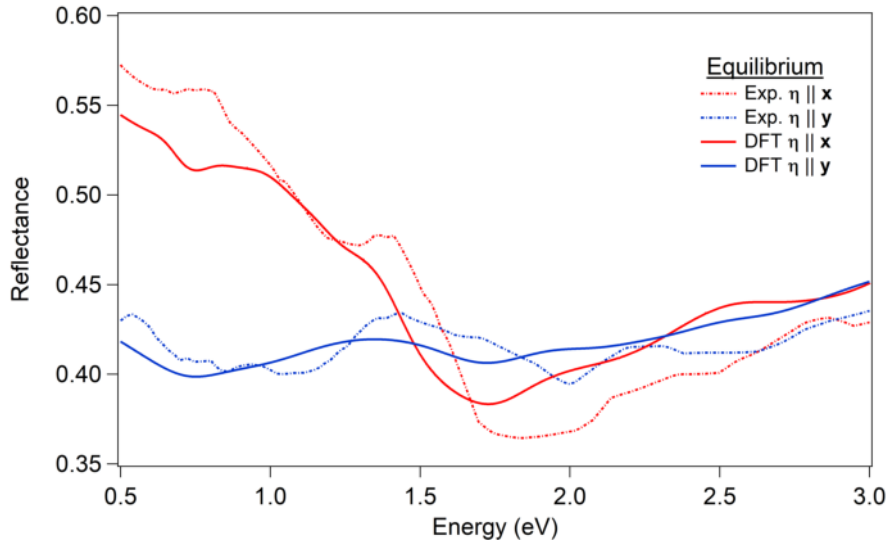

FIG. S14. Equilibrium reflectance curves in the two perpendicular probe polarizations; the experimental curves were derived from the data present in [14] measured at 10 K.

3.2 - Coherent optical phonon effects on the energy levels

The subpicometer atomic displacements in the out-of-equilibrium structural configurations lead to modifications of the electronic band structure (Fig. S15) of the order of a few meV.

Such variations are small, but beyond our relative numerical accuracy. Furthermore, we checked that these effects are almost linear with the displacements if we increase them by a factor up to twenty. We focus on the extrema of the electron and hole bands along Γ-X. In Fig. S16, we show the results corresponding to the displacements estimated from the low
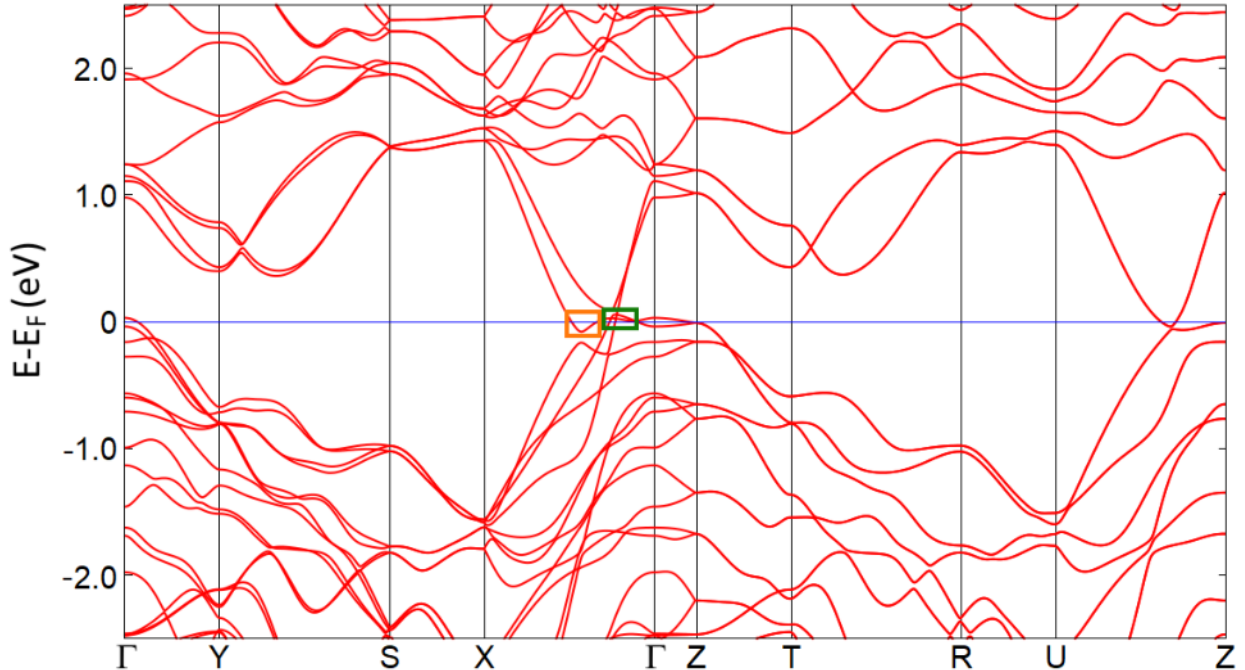
FIG. S15. Electronic band structure of WTe_2 in the equilibrium configuration; the orange and green rectangles highlight respectively the electron and hole pockets; the energy values are referred to the Fermi energy (E_F).

($\sim$230 µJ/cm^2) fluence measurements and reported in the main paper. The effects (doubled in the graph for clarity) depend on the band and phonon mode. For the 8 cm^{-1} mode, the bottom (top) of the electron (hole) band at -80 meV (60 meV) under (above) the Fermi energy experiences a $\sim$0.7 (1.5) meV difference between the two oscillation phases (0 and π, represented in Fig. S17), while for the 80 cm^{-1} modes the difference becomes $\sim$1.7 (0) meV. By properly tuning the Fermi level, these variations, although small, could have an impact on the extremely high magnetoresistance in WTe_2 [16], which is ascribed to a delicate balance between electron and hole carriers. Additional contributions may come from carrier mobility and the magnetic field [17] [18]. We caution the reader that, as stated in the main paper, we used scalar relativistic pseudopotentials. The inclusion of spin-orbit coupling (SOC) using fully relativistic pseudopotentials would provide a more accurate description of these effects, since it is known that SOC plays an important role on the electronic bands around the Fermi level in WTe_2 [19].
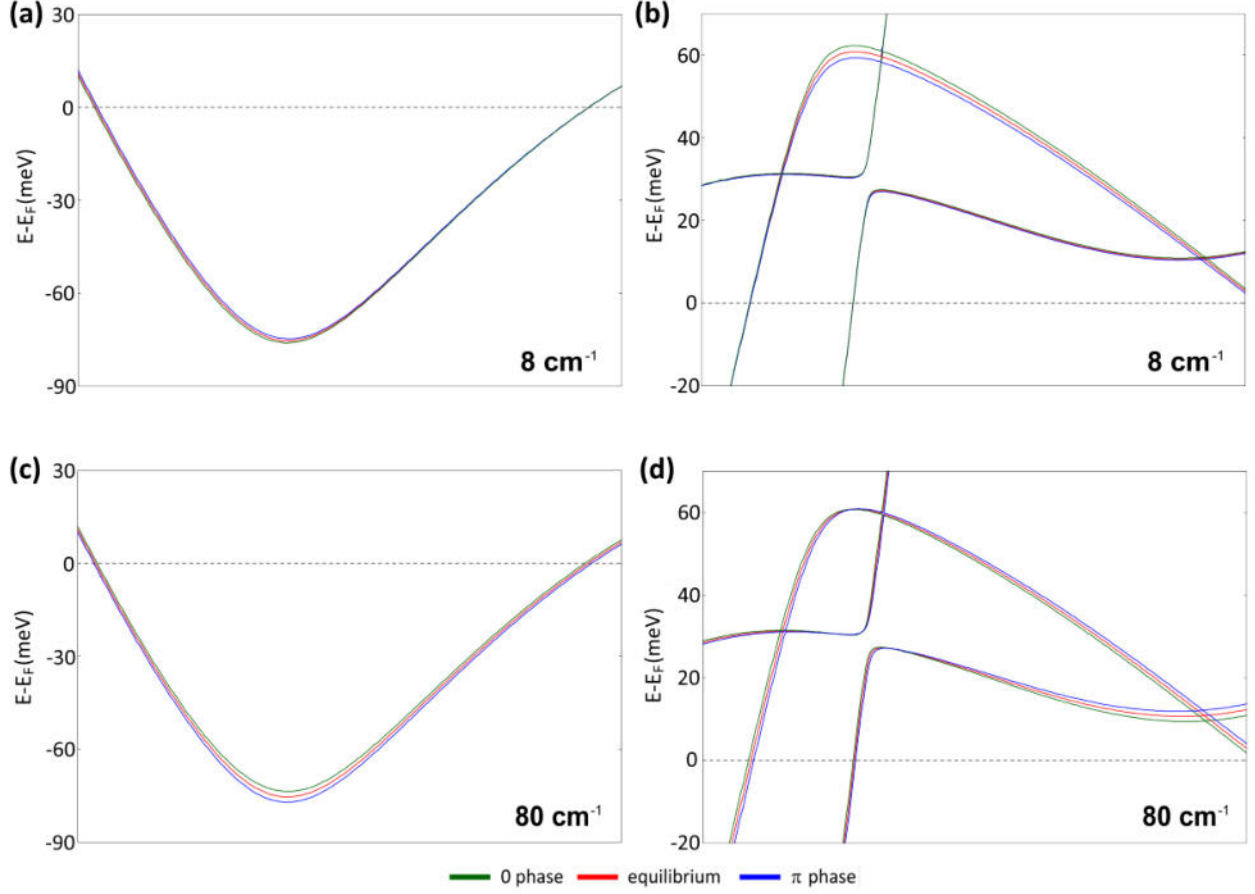
FIG. S16. Effect of the phonon displacements on electron- and hole-like bands cut by the Fermi level along $\Gamma - X$. (a),(b) Magnified views of the regions delimited by the orange and green rectangles in Fig. S15 for the 8 cm^{-1} optical phonon mode; (c),(d) as (a),(b), but for the 80 cm^{-1} phonon mode; the 0 and π phases are labeled as in the main paper, taking as reference the $\eta||\mathbf{x}$ polarization; the displacements used for the graphs are double with respect to the low fluence values reported in the main paper to highlight the phonon effects.

3.3 - Bands contribution to the response function

To accurately describe the effects induced by the optical phonons, it is necessary to include in the response function an appropriate number of bands around the Fermi level. The "converged" curves shown in Fig. S18 were obtained including 119 bands, which is safe enough compared with the 184 electrons per unit cell and the spectral range under consideration for the transitions. In the same figure, we show the effect of varying the number of "conduction bands", i.e. the totally unoccupied bands above the Fermi level.
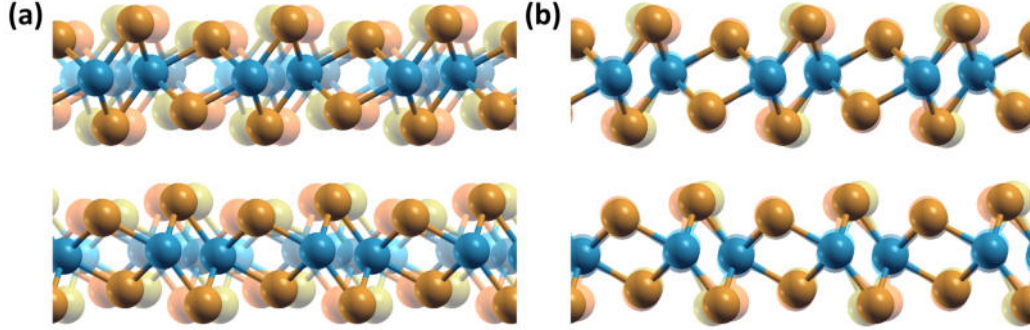
16

FIG. S17. The 0 and π phases of the phonon oscillations for the (a) 8 cm^{-1} mode and (b) 80 cm^{-1} mode. The 0 phase is represented with transparent yellow Te atoms and light blue W atoms, while the π phase is reported with transparent orange Te atoms and dark blue W atoms. Opaque colors describe the atoms in their equilibrium positions. The displacements are exaggerated for a better visualization.

We notice that the main features of the DR/R profile are quickly captured even using few conduction bands, while to correctly compare the DFT amplitudes with the experimental data and give a reasonable estimate of the ionic displacements, more than 15 conduction bands have to be included.

However, since major features are still retained adding only the first conduction band in the response function, we deduce that transitions having final states that belong to bands crossing the Fermi level are involved. This supports the claim that for this material the phonon effects cannot be attributed to single transition in k-space, but to multiple contributions.
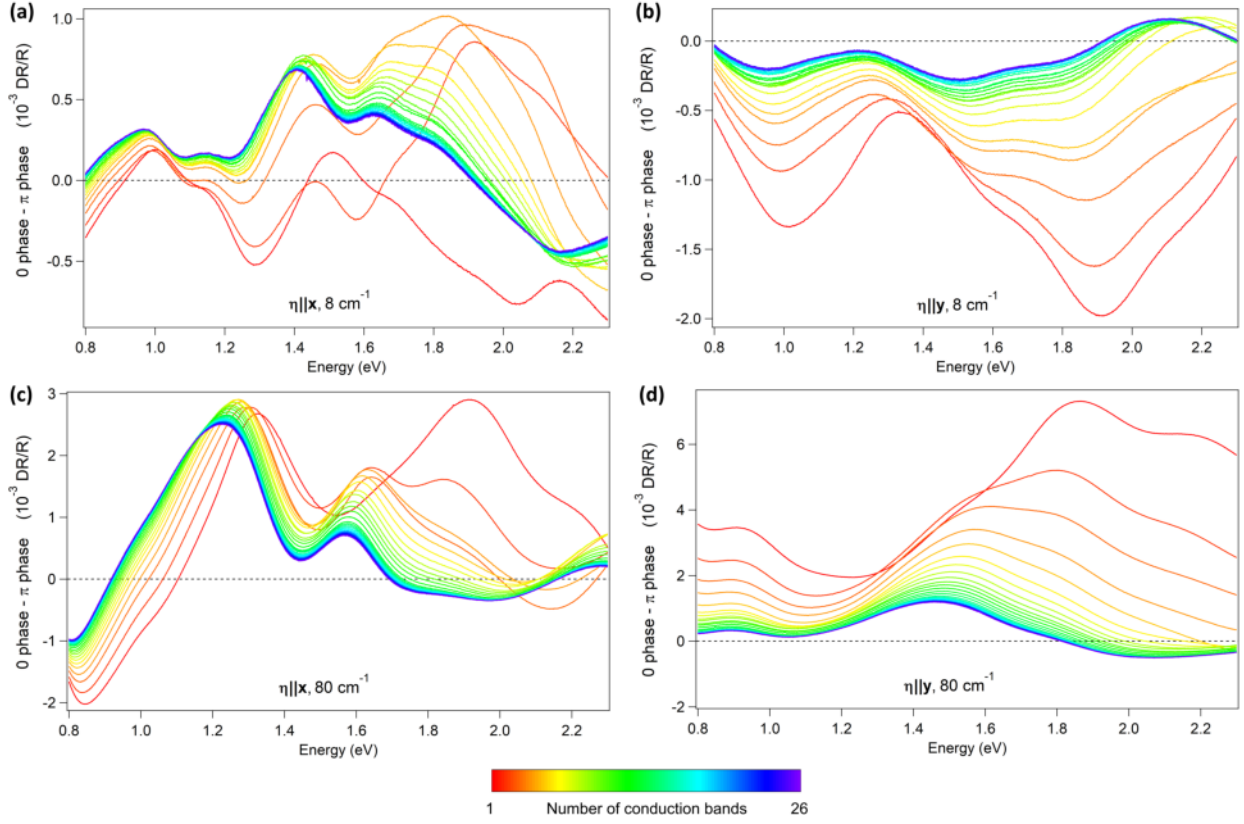
FIG. S18. Phonon effects on the DR/R profile obtained from the differences between the 0 and π phases with an increasing number of conduction bands inserted in the response function; (a) 8 cm^{-1} $\eta||\mathbf{x}$; (b) 8 cm^{-1} $\eta||\mathbf{y}$; (c) 80 cm^{-1} $\eta||\mathbf{x}$; (d) 80 cm^{-1} $\eta||\mathbf{y}$.

* e-mail:federico.cilento@elettra.eu

[1] A. Mar, S. Jobic, and J. A. Ibers, Journal of the American Chemical Society **114**, 8963 (1992).

[2] A. Kokalj, Journal of Molecular Graphics and Modelling **17**, 176 (1999).

[3] F. Wooten, "Optical properties of solids," (Academic Press, New York, 1972) Chap. 3.

[4] B. He, C. Zhang, W. Zhu, Y. Li, S. Liu, X. Zhu, X. Wu, X. Wang, H. Wen, and M. Xiao, Scientific Reports **6**, 30487 (2016).

[5] W.-D. Kong, S.-F. Wu, P. Richard, C.-S. Lian, J.-T. Wang, C.-L. Yang, Y.-G. Shi, and H. Ding, Applied Physics Letters **106**, 081906 (2015).

[6] M. Ligges, I. Rajkovic, P. Zhou, O. Posth, C. Hassel, G. Dumpich, and D. von der Linde, Applied Physics Letters **94**, 101910 (2009).

[7] D. R. Hamann, M. Schlüter, and C. Chiang, Phys. Rev. Lett. **43**, 1494 (1979).

[8] T. Takeda, Zeitschrift für Physik B Condensed Matter **32**, 43 (1978).

[9] J. P. Perdew, J. A. Chevary, S. H. Vosko, K. A. Jackson, M. R. Pederson, D. J. Singh, and C. Fiolhais, Phys. Rev. B **46**, 6671 (1992).

[10] D. R. Hamann, Phys. Rev. B **88**, 085117 (2013).

[11] M. van Setten, M. Giantomassi, E. Bousquet, M. Verstraete, D. Hamann, X. Gonze, and G.-M. Rignanese, Computer Physics Communications **226**, 39 (2018).

[12] P. Giannozzi, S. Baroni, N. Bonini, M. Calandra, R. Car, C. Cavazzoni, D. Ceresoli, G. L. Chiarotti, M. Cococcioni, I. Dabo, A. Dal Corso, S. de Gironcoli, S. Fabris, G. Fratesi, R. Gebauer, U. Gerstmann, C. Gougoussis, A. Kokalj, M. Lazzeri, L. Martin-Samos, N. Marzari, F. Mauri, R. Mazzarello, S. Paolini, A. Pasquarello, L. Paulatto, C. Sbraccia, S. Scandolo, G. Sclauzero, A. P. Seitsonen, A. Smogunov, P. Umari, and R. M. Wentzcovitch, Journal of Physics: Condensed Matter **21**, 395502 (2009).

[13] A. Marini, C. Hogan, M. Grüning, and D. Varsano, Computer Physics Communications **180**, 1392 (2009).

[14] A. J. Frenzel, C. C. Homes, Q. D. Gibson, Y. M. Shao, K. W. Post, A. Charnukha, R. J. Cava, and D. N. Basov, Phys. Rev. B **95**, 245140 (2017).

[15] C. C. Homes, M. N. Ali, and R. J. Cava, Phys. Rev. B **92**, 161109 (2015).

[16] M. N. Ali, J. Xiong, S. Flynn, J. Tao, Q. D. Gibson, L. M. Schoop, T. Liang, N. Haldolaarachchige, M. Hirschberger, N. P. Ong, and R. J. Cava, Nature **514**, 205 (2014).

[17] Y. L. Wang, L. R. Thoutam, Z. L. Xiao, J. Hu, S. Das, Z. Q. Mao, J. Wei, R. Divan, A. Luican-Mayer, G. W. Crabtree, and W. K. Kwok, Phys. Rev. B **92**, 180402 (2015).

[18] M. Trescher, E. J. Bergholtz, M. Udagawa, and J. Knolle, Phys. Rev. B **96**, 201101 (2017).

[19] A. A. Soluyanov, D. Gresch, Z. Wang, Q. Wu, M. Troyer, X. Dai, and B. A. Bernevig, Nature **527**, 495 (2015).